Tunable Bandpass Filter With Serially Coupled Ring Resonators Assisted MZI

Niharika Kohli, Bruno Lee Sang, Frédéric Nabki, *Member, IEEE*, and Michaël Ménard, *Member, IEEE*

***Abstract*—We present the analytical modelling and experimental characterization of a new design of silicon nitride tunable bandpass filter based on serially coupled ring resonators assisted Mach-Zehnder interferometer (SR-MZI). SR-MZI filters provide an additional degree of freedom to independently control the bandwidth and shape of the passband as compared to previous ring-assisted MZI filters. It is possible to tune the bandwidth, shape and side-band rejection of the response by adjusting the coupling in the filters, providing a scope for fully reconfigurable performance. The fabrication of the filters is CMOS compatible and supports mass production. Preliminary results for thermal controllability are presented.**

***Index Terms*—Bandpass filters, serial rings, ring-assisted MZI, Integrated photonics, silicon nitride waveguides.**

I. Introduction

INTEGRATED optical filters are among the most widely used components in photonic circuits. Many optical applications utilize interferometric devices such as Mach-Zehnder Interferometer (MZI) [1], [2], Ring Resonators (RRs) [3]–[7], Bragg or Arrayed Waveguide Gratings (AWGs) [8]–[10], contra-directional couplers [11], [12] and photonic crystal filters [13] for their filtering requirements.

One common application of optical filters is to isolate frequency channels in wavelength division multiplexed (WDM) networks used in data communication and telecommunication systems [1], [8], [11], [14]. The ever-increasing demand for bandwidth in these systems has brought forward the need for gridless networks, also known as elastic optical networks (EONs), where the channel spacings and bandwidth can be adjusted dynamically. EONs are needed to maximize the available bandwidth and prevent wastage of spectrum [15]. To be useful in EONs, the filter should be dynamic such that it is able to adapt to the ongoing traffic requirements. Additionally, these filters should have low insertion loss, a box-like response, and a high extinction ratio and side-band rejection.

Many design strategies to implement optical filters with an optimized passband response have been proposed in the literature [14], [16] and the past decade has seen growing interest in reconfigurable bandpass filters (BPFs) with tunable bandwidth and central wavelength [17]–[23]. Ring resonators are the most commonly used components in these filters since they are easy to fabricate and have a small footprint. One promising approach to implement a tunable BPF is the Ring Assisted Mach-Zehnder interferometer (RA-MZI) with one or more ring resonators (RRs) embedded in one or both of its arms [16], [20], [23], [24]. This configuration offers a more box-like passband response compared to cascaded RRs without the MZI [19], [21], [22]. However, as the number of rings increases in these RA-MZI filters, the tuning mechanism to achieve the optimum shape for the filter becomes more and more complex [23], [24]. In this study, we analyzed two different coupling configurations between the RRs and MZI in which two RRs are coupled in series or in parallel to the MZI. To the best of our knowledge, this is the first time that a BPF was implemented by combining Serially coupled Rings and a MZI (SR-MZI). Moreover, we observed that the SR-MZI filter offers several advantages compared to the parallel coupling configuration [20]; specially in terms of the shape of the bandpass response and the degrees of freedom to optimize the various performance parameters.

We used Silicon Nitride (SiN) strip waveguides surrounded with a Silicon Dioxide (SiO_2) cladding to implement our filter designs. SiN photonics platforms have received considerable attention recently owing to the superior performance of SiN as an optical material for passive devices [2], [6], [9], [25]–[27]. SiN offers small optical propagation losses and high transparency at visible and near infrared wavelengths. Additionally, SiN does not suffer from two photons and free carrier absorption at telecommunication wavelengths.

In Section II, we present the analytical modelling of RA-MZIs in serial and parallel configurations followed by a comparison of their theoretical responses. The effect of the coupling coefficients between the two RRs and between the RRs and MZI is shown on the pole-zero plots and transmission responses. Superior performance with the flexibility to tune the shape of the filter response to make it more box-like is obtained for the proposed SR-MZI filter. In Section III, experimental results from the fabricated SR-MZI devices are presented. The experimental

Manuscript received June 2, 2021; revised July 29, 2021; accepted August 3, 2021. Date of publication August 10, 2021; date of current version August 27, 2021. The authors would like to acknowledge NSERC and PRIMA Québec for their financial support and AEPONYX for the fabrication of the prototypes and their financial support. *(Corresponding author: Niharika Kohli.)*

Niharika Kohli was with the Department of Electrical Engineering, École de Technologie Supérieure, Montréal, QC H3C 1K3, Canada. She is now with CMC Microsystems, Montréal, QC H3C 6M8, Canada. (e-mail: niharika.kohli@cmc.ca).

Frédéric Nabki is with the Department of Electrical Engineering, École de Technologie Supérieure, Montréal, QC H3C 1K3, Canada (e-mail: frederic.Nabki@etsmtl.ca).

Bruno Lee Sang is with the AEPONYX Inc., Montréal, QC H3C 2M7, Canada (e-mail: bruno.leesang@aeponyx.com).

Michaël Ménard is with the Department of Computer Science, Université du Québec à Montréal, Montréal, QC H2X 3Y7, Canada (e-mail: menard.michael@uqam.ca).

Digital Object Identifier 10.1109/JPHOT.2021.3103142

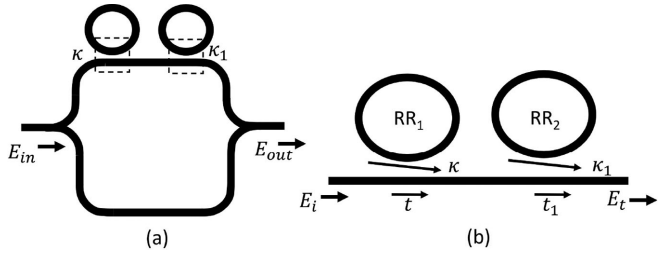

Fig. 1. (a) Schematic for Design 1 with parallel coupling between two rings and a MZI. (b) Schematic of cascaded rings RR_1 and RR_2 and the MZI bus waveguide used in (a). t, t_1 and κ, κ_1 represent the field transmission and coupling coefficients between the rings and the MZI.

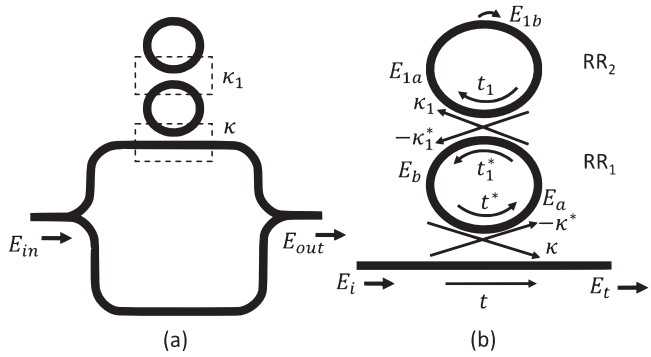

Fig. 2. (a) Schematic for Design 2 with serial coupling between two rings and MZI. (b) Schematic of cascaded rings RR_1 and RR_2 and the MZI bus waveguide used in (a). κ, κ_1 and t, t_1 represent the field coupling and transmission coefficient between the RR_1 and MZI and RR_1 and RR_2, respectively.

results match well with the theoretical responses for different values of coupling coefficients in the SR-MZI filter. The results also show the possibility of tuning the bandwidth of the SR-MZI filters using thermo-optic effect.

II. Device Design

A. Analytical Modelling of RA-MZI Configurations

Fig. 1 shows the first RA-MZI configuration (Design 1) that can be used to obtain a bandpass response with two rings [20]. The rings are coupled in parallel to the shorter arm of the MZI as shown in Fig. 1(b). The field transmission and coupling coefficients between the MZI and the RRs are represented by (t, t_1) and (κ, κ_1) respectively. For lossless coupling, which is assumed here, $t^2 + \kappa^2 = 1$. The explanation for deriving the transfer function, H(z), for this configuration is provided in Appendix A. For lossless waveguides, H(z) can be represented as the ratio of two third-order polynomials:

$$H(z) = \frac{tt_1z^3 + [1-(t+t_1)]z^2 + [1-(t+t_1)]z + tt_1}{2z[z^2 - (t+t_1)z + tt_1]} \quad (1)$$

The roots of the numerator and denominator determine the zeros and poles of the transfer function which ultimately determine the response of the filter. It is interesting to note that two identical rings have the same effect on the response of the filter and therefore, the transmission coefficients t and t_1 are interchangeable in (1). The effect of the transmission coefficients on the pole-zero plot of such a filter is presented in the following section.

The proposed configuration (Design 2), which is the focus of this work, is a SR-MZI in which the two RRs are coupled to the MZI in series, as shown in Fig. 2(a). To the best of our knowledge, this configuration has not been investigated as a bandpass filter in the past. Fig. 2(b) shows a schematic of the MZI bus waveguide with the serially coupled RRs used in this filter. The various electric field components, field transmission and coupling coefficients are also shown. The derivation of the transfer function, H(z), for this configuration is provided in Appendix B.

For lossless waveguides, the overall transfer function is expressed as the ratio of two third-order polynomials as follows:

$$H(z) = \frac{tz^3 + [1-t_1(1+t)]z^2 + [1-t_1(1+t)]z + t}{2z[z^2 - t_1(1+t)z + t]} \quad (2)$$

There is a fundamental difference between the transfer function of Design 1 in (1) and this expression. Unlike in Design 1, the transmission coefficients t and t_1 do not have the same effect on the filter response. We will show in the next section that it adds an additional degree of freedom to optimize the response of the filter.

B. Theoretical Filter Responses

In the two RA-MZI configurations discussed above, the RRs are coupled to the shorter arm of the MZI and the circumference of each RR is equal to the difference in length between the two arms of the MZI. This length has been optimized such that the Free Spectral Range (FSR) of the rings and the MZI is equal to 200 GHz ($1.6\,nm$ at a wavelength of $1550\,nm$). This FSR was chosen only to demonstrate the concept and it can be increased by reducing the size of the rings [28]. However, the minimum bending radius that can be used is limited by the bending loss of the waveguides. Because the TE and TM polarizations have slightly different modal properties, we first chose to optimize all the designs for the TE polarization at a wavelength of $1598\,nm$. A polarization diverse architecture combining a polarization splitter with two instances of our RA-MZI each optimized for the TE and TM polarizations is the subject of ongoing work.

The effect of the various coupling coefficients on the poles and zeros of the filter, and thus on its response, has been investigated through numerical simulations. For Design 1, as shown in (1), the transmission coefficients t and t_1 have the same effect on the transfer function. Fig. 3 shows the pole-zero plots and the corresponding transmission responses for this filter when the coupling coefficient, $\kappa = \sqrt{(1-t^2)}$ is equal to 0.5, 0.7 and 0.9 and $\kappa_1 = 0.9$.

The pole-zero plot shows that the two complex zeros of the system moves outwards on the unit circle while one of the poles move away from the unit circle when the coupling coefficient, κ, is increased. The outward rotation of the zeros on the unit circle increases the bandwidth of the filter and the movement

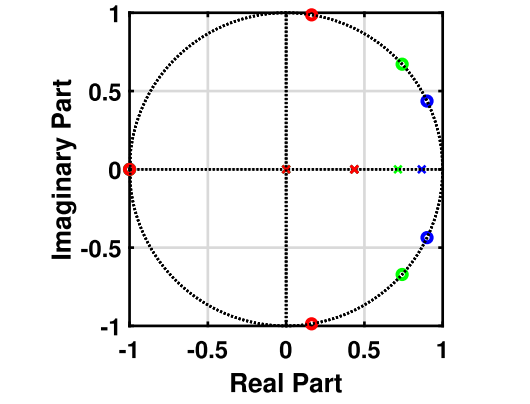

(a)

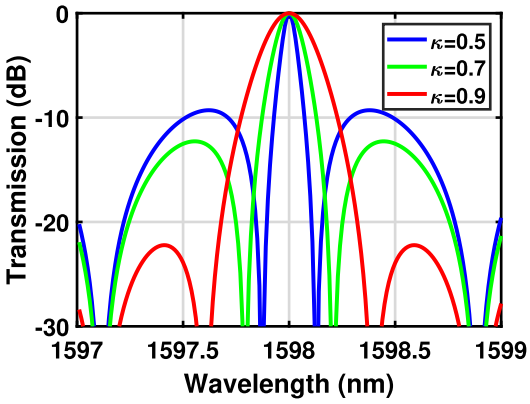

(b)

Fig. 3. (a) Pole-zero diagram for Design 1 for $\kappa_1 = 0.9$ and $\kappa = 0.5$ (blue), $\kappa = 0.7$ (green), $\kappa = 0.9$ (red). (b) Simulated transmission response for Design 1. Increasing κ provides a smaller slope in the transition regions, a higher bandwidth and a higher side-band rejection.

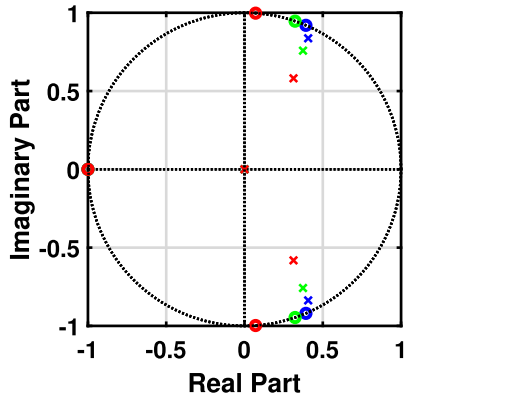

(a)

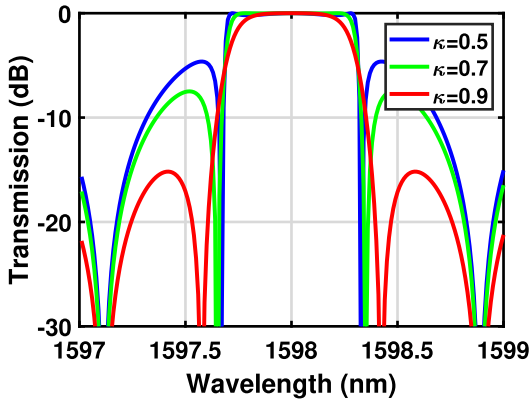

(b)

Fig. 4. (a) Pole-zero diagram for Design 2 (SR-MZI) for $\kappa_1 = 0.9$ and $\kappa = 0.5$ (blue), $\kappa = 0.7$ (green), $\kappa = 0.9$ (red). (b) Simulated transmission response for this SR-MZI filter. Increasing κ provides smaller slope of transition regions and higher side-band rejection.

of the pole away from the unit circle decreases the slope of the passband. Therefore, variations in coupling between the rings and the MZI simultaneously changes the bandwidth and slope of the transition regions around the passband. This can be observed in the transmission response in Fig. 3.

On the other hand, as shown in (2), the coupling coefficient between RR_1 and the MZI, $\kappa = \sqrt{(1-t^2)}$, and between RR_2 and RR_1, $\kappa_1 = \sqrt{(1-(t_1)^2}$, in the SR-MZI (Design 2) have different impacts on the response of the filter. Fig. 4 shows the pole-zero plot and the corresponding wavelength response of the SR-MZI filter when κ is equal to 0.5, 0.7 and 0.9 and $\kappa_1 = 0.9$. Two of the poles of the system are complex conjugates of each other and one of the poles is always at zero. It can be observed from the pole-zero plot that as κ increases, the zeroes move outward on the unit circle by a much smaller distance than in Design 1. The two complex poles of the system simultaneously move away from the unit circle, which decreases the slope of the transition regions. Therefore, as shown in the filter transmission response in Fig. 4, varying κ changes the slope of the transition regions (slope smaller for higher κ) while maintaining the same 5-dB bandwidth.

By changing κ_1 (i.e. the coupling between the rings) in the SR-MZI filter, we obtain the pole-zero plots and transmission responses shown in Fig. 5. When κ_1 increases, the zeros of the system move outward on a circle of unit radius. Also, the complex poles of the system move outward on a circle of radius equal to the transmission coefficient t. As mentioned before, the outward movement of the zeroes increases the bandwidth of the passband, which is confirmed in the transmission responses shown in Fig. 5. The distance between the poles and the unit circle is fixed, therefore, the slope of the passband does not change with changes in κ_1. It is also important to note from Fig. 3–5 that the side-band rejection always increases when the coupling coefficients increase.

This independent control to optimize the bandwidth and slope of the filter passband offers an additional degree of freedom in SR-MZI filters. For example, if a filter is designed for a specific bandwidth, the slope of the passband can be optimized according to the specifications needed for the filter. The Shape Factor (SF), which is defined as the ratio of the 1-dB over the 10-dB bandwidth, can be used to evaluate the slope or the box-like behavior. A higher SF means a more box-like response. A high value of SF can potentially reduce the crosstalk from adjacent channels in WDM systems. It also makes the system more tolerant to small drifts in wavelength. Similarly, a higher side-band rejection is beneficial for such filters.

This flexibility is further emphasized in Fig. 6 which shows the transmission response for both Design 1 and 2 for a 3-dB bandwidth of $0.14\,nm$. The values of the coupling coefficients in Design 1 to obtain this bandwidth are $\kappa = \kappa_1 = 0.82$. On

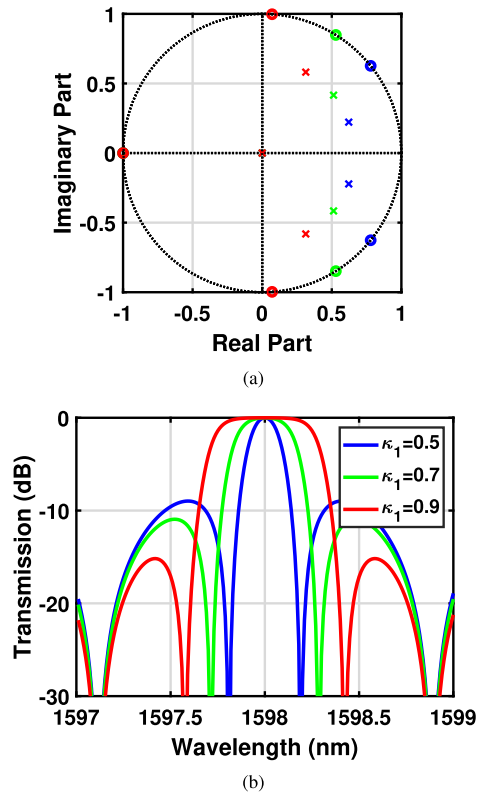

Fig. 5. (a) Pole-zero diagram for Design 2 (SR-MZI) for $\kappa = 0.9$ and $\kappa_1 = 0.5$ (blue), $\kappa_1 = 0.7$ (green), $\kappa_1 = 0.9$ (red). (b) Simulated filter response for this SR-MZI filter. Increasing κ_1 provides higher bandwidth and side-band rejection.

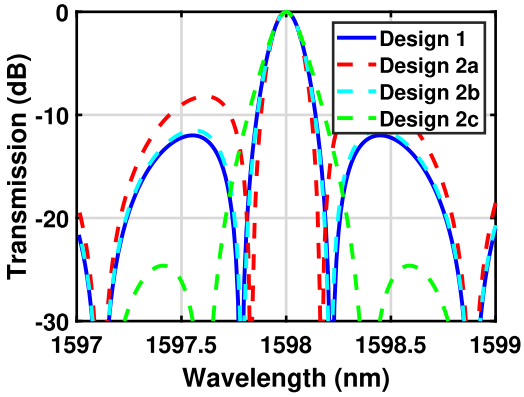

Fig. 6. Simulated transmission response shown with dashed lines for Design 2 (SR-MZI) when the values of the field coupling coefficients are optimized to achieve a 3-dB bandwidth of $0.14\,nm$ as in Design 1. Design 2a : $\kappa = 0.89$ and $\kappa_1 = 0.45$, Design 2b: $\kappa = 0.94$ and $\kappa_1 = 0.5$, Design 2c: $\kappa = 0.99$ and $\kappa_1 = 0.6$. The response for Design 1 with $\kappa = \kappa_1 = 0.82$ is shown in the solid blue line.

the other hand, with Design 2 (SR-MZI) we can obtain this bandwidth with various combinations of κ and κ_1 corresponding to different SF and side-band rejection. For $\kappa = 0.94$ and $\kappa_1 = 0.5$, the response of Design 2b is identical to Design 1, providing a SF of 0.34. In Design 2a, for $\kappa = 0.89$ and $\kappa_1 = 0.45$, the SF increases from 0.34 to 0.38 at the expense of the side-band rejection which decreases from 12 dB to 8 dB. On the other hand, if we increase κ from 0.94 to 0.99 and κ_1 from 0.5 to 0.6, we can achieve the same bandwidth with a higher side-band rejection of 25 dB at the expense of a smaller SF of 0.25 in Design 2c. Clearly, there is a trade-off between the side-band rejection and the shape-factor. This example illustrates the benefit of SR-MZI filters (Design 2) in terms of the potential to optimize the shape factor and side-band rejection of the filter according to the application needs.

III. Experimental Results

The SR-MZI filter designs were implemented using trapezoidal SiN strip waveguides with a side-wall angle of 86°. The thickness of the waveguide was $440\,nm$ and the design width was close to $450\,nm$ in all designs. The fabrication process started with a TEOS Low-Pressure Chemical Vapor Deposition (LPCVD) of a $3.2\,\mu m$ thick SiO_2 layer on the silicon wafer. Next, a silicon rich SiN layer of $440\,nm$ was deposited using LPCVD. The SiN waveguide pattern was then defined using UV lithography in a stepper followed by dry etching. Finally, a $3.2\,\mu m$ thick SiO_2 cladding was deposited using TEOS Plasma Enhanced Chemical Vapor Deposition (PECVD). The fabrication of these devices was carried out by our industrial collaborators at a commercial foundry.

These SR-MZI filters were fabricated in two different runs: one without metal heaters and the other with Aluminum Copper (AlCu) metal heaters. Fig. 7 shows an optical microscope photograph of the fabricated SR-MZI filters in both runs. The first version was based on circular RRs as shown in Fig. 7(a) and the second version with metal heaters was based on race-track RRs as shown in Fig. 7(b). The race-track RRs were used to increase the length of the coupling region between the rings such that heaters can be used on top of this region to tune the coupling coefficients to compensate fabrication variations. Therefore, in this case the FSR of the filter was 100 GHz compared to 200 GHz in the first version. Heaters were also placed on top of the individual RRs and MZI to tune the relative phase-shift between them in order to optimize the shape of the response of the filter after fabrication.

Light was coupled in and out of the chip through surface grating couplers and the measured responses were normalized with respect to the grating response using reference structures in order to remove the wavelength dependent coupling losses. The MZI in the SR-MZI had 3-dB multimode interference (MMI) couplers at the input and output. The extinction ratio of the filters was limited by the splitting ratio of the MMI couplers, which can be further optimized for a better performance. Experimental results for the TE mode of the SR-MZI prototypes in both runs are presented below. The simulation results using Lumerical FDTD and MODE solvers [29] are also provided for comparison with the experimental results.

A. Experimental Results for Different Coupling Gaps

In the SR-MZI filters fabricated in the first run, different gaps were used between the MZI and RR_1 and between the two RRs to validate our model and show the effect of the coupling on the response of the filter. Fig. 8 shows the measured transmission response (blue-dashed) and its comparison with the simulated response (red-solid) for these filters. Due

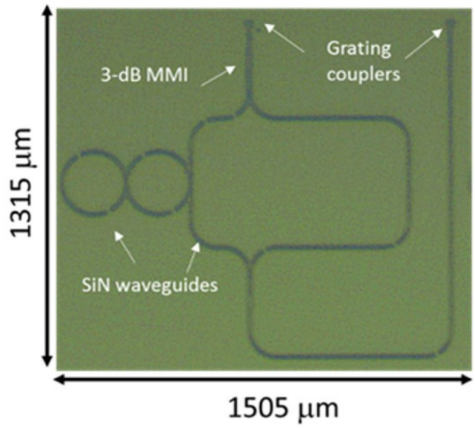

(a)

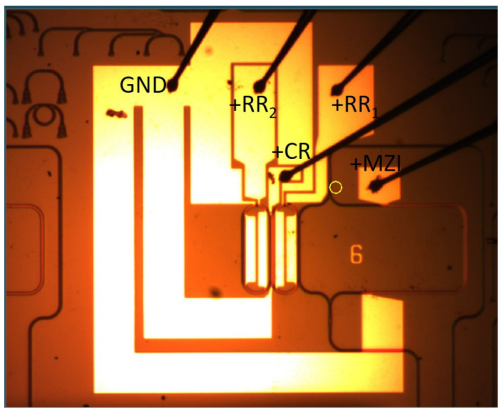

(b)

Fig. 7. Optical microscope photograph of fabricated SR-MZI filters in the two runs. (a) Run-1: SR-MZI with FSR = 200 GHz and circular rings. (b) Run-2: SR-MZI filter with FSR = 100 GHz, race-track rings and metal heaters on top.

to fabrication variations, the phase of the RRs and MZI are not identical, which leads to asymmetry in the sidebands of the measured responses. These variations can be compensated by tuning the phase-shifts of the MZI and RRs using thermal heaters, which were not present in the first run. The extinction ratio in the simulated response was also decreased to match the measured response by changing the splitting ratio at the input and output of the MZI. The worst-case splitting ratio used was 60/40. The simulated response match well with the measured response. However, a slight discrepancy in the bandwidth and FSR can be seen which can be attributed to small variations around the fabrication tolerances in the various parameters used in the simulation. The measured 3-dB bandwidth for the three devices was found to be a) $0.82\,nm$ (for MZI-RR_1 gap $= 900\,nm$, RR_1-RR_2 gap $= 600\,nm$), b) $0.9\,nm$ (for MZI-RR_1 gap $= 1100\,nm$, RR_1-RR_2 gap $= 600\,nm$) and c) $0.54\,nm$ (for MZI-RR_1 gap $= 1100\,nm$, RR_1-RR_2 gap $= 800\,nm$). The values of coupling coefficient corresponding to these gaps were calculated from FDTD simulations and are shown in the figure labels. The bandwidth variation in these devices agrees with the theoretical prediction that a reduction in coupling between the rings decreases the bandwidth significantly, as seen in device (b) and (c). It can also be observed from Fig. 8 that for a lower coupling between the MZI and RR_1, the response is more box-like compared to a higher coupling, as seen in device (a)

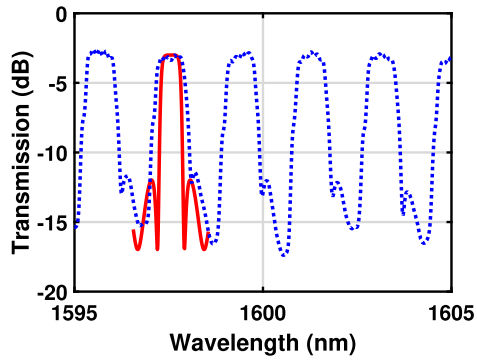

(a)

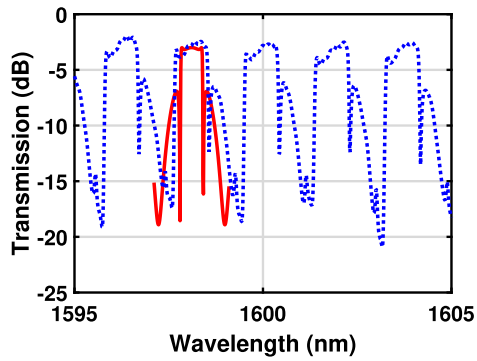

(b)

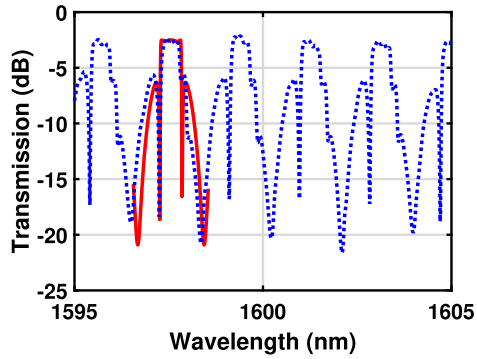

(c)

Fig. 8. Normalized measured TE response for three SR-MZI filter devices and its comparison with the theoretical response. (a) Device 1: Gap between RR_1 and MZI $= 900\,nm$ ($\kappa = 0.83$) and gap between RRs $= 600\,nm$ ($\kappa_1 = 0.87$). (b) Device 2: Gap between RR_1 and MZI $= 1100\,nm$ ($\kappa = 0.48$) and gap between RRs $= 600\,nm$ ($\kappa_1 = 0.87$) c) Device 3: Gap between RR_1 and MZI $= 1100\,nm$ ($\kappa = 0.48$) and gap between RRs $= 800\,nm$ ($\kappa_1 = 0.85$). Waveguide width $= 460\,nm$ and FSR $= 200$ GHz in all designs. Dashed-Measurement, Solid- Simulation.

and (b). The measured insertion losses of the filters in all three cases were found to be lower than 3-dB.

B. Experimental Results With Thermal Tuning

The second run provided the opportunity to implement thermo-optic heaters. They were used to change the coupling coefficients between the rings by strategically placing them over the coupling regions between the waveguides [30], [31] to tune the bandwidth of the SR-MZI filter and to compensate for fabrication variations affecting the coupling coefficients. In the second fabrication run, a $250\,nm$ thick layer of AlCu was sputtered on the top-cladding and then wet-etched to pattern

$15\,\mu m$ wide heater wires on top of the waveguides. From simulations carried out with Lumerical MODE solver, we found that the effective index of the waveguide, including its imaginary part, is not affected by the metal heaters placed at a vertical separation of $3.2\,\mu m$ from the SiN waveguide. Therefore, no additional losses are introduced due to the heaters in this device.

To estimate the coupling between the RRs of the SR-MZI filter, we also fabricated simple directional couplers (DC) with the same length and gaps as in the racetrack RRs used in the SR-MZI. Heaters were fabricated on top of the coupling regions in the directional couplers and over the coupling region between the two racetrack RRs of the SR-MZI to tune the coupling coefficients. Heaters were also fabricated on top of the MZI, RR_1 and RR_2 waveguides in the SR-MZI filters to independently tune the phase-shifts in these components.

The range of thermal tuning of the coupling coefficient depends on various parameters of the coupled waveguides, such as the gap between the waveguides and the length of the coupler [30], [32]. In the SR-MZI, we used a gap of $2.2\,\mu m$ between the racetrack RRs and the length of the coupling region in these RRs was $440\,\mu m$. For these parameters, we were able to obtain a coupling variation of up to 17% in the directional couplers as shown in the results below. The limited thermal tuning is due to a relatively small coupling length of $440\,\mu m$. As shown in [32] much higher lengths are required for highly tunable SiN directional couplers. Nevertheless, as discussed below, there is still scope for improving the range of tuning further by increasing the gap between the waveguides and the length of the coupling region. Furthermore, the tuning efficiency and range could be improved by creating isolating air trenches around the waveguide [33] and/or partially removing the silicon substrate under the heaters to reduce thermal dissipation [34].

Fig. 9(a) and (b) show the normalized measured spectral response of the directional couplers with a coupling length of $440\,\mu m$ and a gap of $2.0\,\mu m$ and $2.2\,\mu m$, respectively, between two straight SiN waveguides. After normalizing with the grating coupler responses, the additional losses including the insertion loss and any active measurement related losses were removed from the measured data for the ease of analysis. It can be observed from the figures that for these gaps, the waveguides are over-coupled, and the gaps should be increased further for better performance. This is because the fabricated waveguides were narrower than the intended design values of $450\,nm$. The simulation results match with the measurements when widths of $\sim 410\,nm$ and $\sim 425\,nm$ were used in Fig. 9(a) and Fig. 9(b), respectively.

We demonstrated tuning of the coupling when voltage is applied to the heater on top of the coupling region (CR). The voltages applied to the CR heater ranged from zero to $1.9\,V$, as shown in Fig. 9. At a wavelength of $1600\,nm$, the variation in coupled power with thermal tuning is 8% for the DC with a gap of $2.0\,\mu m$ and 17% for the DC with a gap of $2.2\,\mu m$. This is because the temperature difference between the two waveguides is higher when the waveguides are separated by a larger gap [30]. The tuning range could be improved since the gaps need to be increased further to optimize the coupling, as mentioned above. The power dissipated corresponding to this coupling variation in

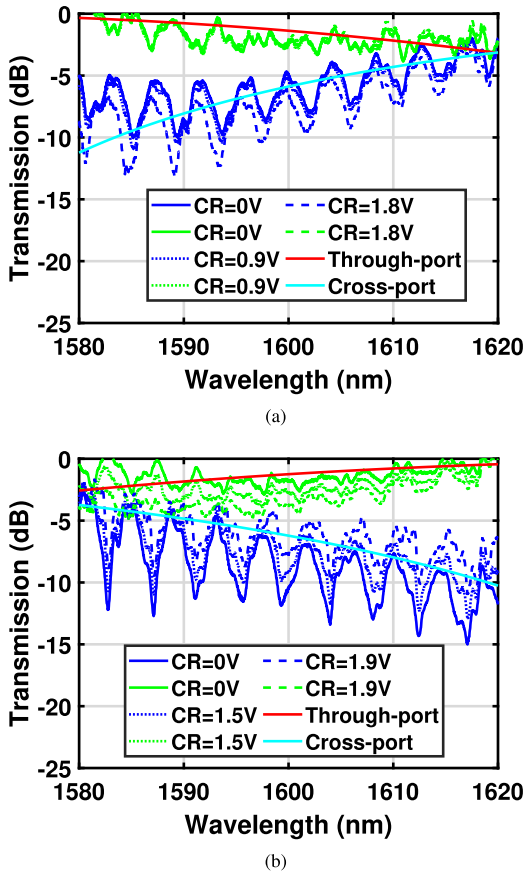

Fig. 9. Normalized measured TE response for directional couplers of length $440\,\mu m$ with thermal tuning. (a) Directional coupler with a gap of $2.0\,\mu m$ between the straight waveguides; width of waveguides in simulation: $424\,nm$ and $429\,nm$. (b) Directional coupler with a gap of $2.2\,\mu m$ between the straight waveguides; width of waveguides in simulation: $410\,nm$ and $415\,nm$. Simulation labels: Through-port; Cross-port.

the two devices is $392\,mW$ (Fig. 9(a)) and $416\,mW$ (Fig. 9(b)), respectively. The current passing through the heater was limited to 220 mA to avoid damaging them. We also show the simulated response of the DC in Fig. 9. There are ripples in the measured spectral responses. We observed that the FSR of these ripples is changing with the measurement setup conditions. Therefore, it can be concluded that these were not caused by reflections in the device itself. The alignment of the fiber array with respect to the grating couplers on the chip appears to be the major contributor to these ripples. We are working on improving the measurement setup and on further improving the design of the grating couplers used in the chips.

Fig. 10 shows the measured and simulated response of SR-MZI filters with a gap of $2.2\,\mu m$ between the RRs and a gap of $2\,\mu m$ between the RR_1 and MZI, and where the length of the coupling regions is $440\,\mu m$. The coupled power between the racetrack RR_1 and RR_2 can be thermally tuned by applying a voltage to the CR heater in the same way as shown in the DC devices above. However, the CR heater also introduces a phase-shift in RR_1 since it is placed on top of the RR_1 waveguide in the coupling region. Therefore, the reference response must also incorporate this phase-shift in RR_1 to ensure that a comparison

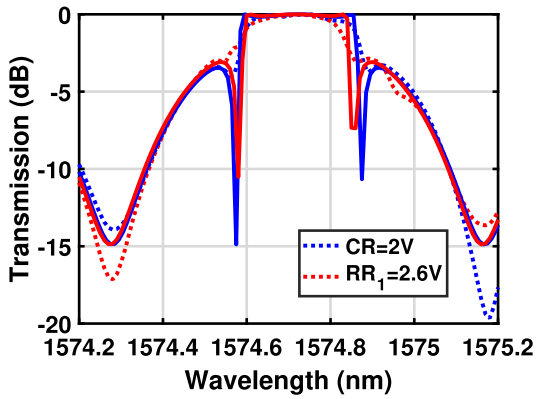

Fig. 10. Thermal tuning of the measured TE response for SR-MZI filter device with gap of $2.2\,\mu m$ between RR_1 and RR_2 and gap of $2\,\mu m$ between the RR_1 and MZI. For simulation, we used $\kappa = 0.45$, and κ_1 was changed from 0.80 to 0.85. Dashed: Measurement; Solid: Simulation.

with the reference response shows only the variations due to the change in the coupling inside the filter. We started by applying a voltage to the CR heater and recorded the spectral response. Then, we switched off the CR heater voltage and applied a voltage to the RR_1 heater to provide the same phase-shift as in the first step. The spectral response in the second step provides the required reference response. These two responses and the corresponding voltages applied to the CR and RR_1 heaters are shown in Fig. 10. The current in RR_1 heater was limited to $200\,mA$ compared to $220\,mA$ in the CR heater because of its shorter length. The power dissipation corresponding to the CR heater was $350\,mW$. The variation in the side-lobe transmission introduced due to the voltage applied to the heaters provides an indication about the phase-shift induced due to the heater. It is also necessary to align the side-lobes of the response by adjusting the phase-shifts in the rings and MZI. In this case, we did not tune any other component to align the side-lobes. However, simultaneous tuning of other components might be necessary in most cases.

This response was recorded at a shorter wavelength because, as shown in the DC response in Fig. 9(b), the coupling is quite small at a wavelength of $1600\,nm$, which reduces the side-band rejections in the response and makes it difficult to analyze the passbands. It can be seen in the response in Fig. 9(b) that the coupling between the waveguides increases with the application of a voltage on the heater. Therefore, as expected, the bandwidth increases with the voltage on the CR heater in Fig. 10 because of the increase in the coupling between the two RRs. The 1-dB bandwidth increases from $0.22\,nm$ to $0.25\,nm$. The simulation result is also shown in the figure in which the power coupling between the RRs was increased from 0.64 to 0.72 to match the experimental response. A slight increase in the side-band rejections can also be observed in the figure corresponding to the increase of the coupling coefficient between the RRs. The lowest insertion loss of the filters without active tuning was around 3 dB. These results show that it is possible to thermally tune the bandwidth and phases in the SR-MZI filter. We believe that with further design optimization and more sophisticated active tuning setup, the reconfiguration capabilities of the filter can be improved further.

IV. Conclusion

We proposed and demonstrated a novel ring-assisted MZI bandpass filter design in which the rings are coupled serially to the MZI. This design offers an additional degree of freedom to independently optimize the bandwidth and box-like shape of the filter compared to the previous RA-MZI designs. An insertion loss of around 3 dB was obtained for the fabricated SR-MZI filters with a design waveguide width and thickness of $450\,nm$ and $440\,nm$, respectively. Despite being made of coupled resonators, the design sensitivity to fabrication variations is low enough to be compensated with thermal tuning. The fabrication was carried out at a commercial foundry and is compatible with CMOS processes. Such filters incorporating mechanisms to dynamically alter their coupling coefficients have the potential to find applications in future elastic optical networks.

Appendix A

A round trip in RR_1 or RR_2 corresponds to a phase of $z^{-1} = e^{-i\beta L}$ where L is the circumference of the RRs and β is the propagation constant of the waveguide. The propagation loss in the rings is given by α. The transfer function of the structure in Fig. 1(b) can be expressed using a Z-transform approach [35] as a product of the transfer functions of the two rings:

$$H_{RR}(z) = \frac{(t - \alpha z^{-1})(t_1 - \alpha z^{-1})}{(1 - \alpha t z^{-1})(1 - \alpha t_1 z^{-1})} \tag{3}$$

The overall transfer function of the filter in Fig. 1(a) can be expressed in terms of the addition of transfer functions in both arms of the MZI as:

$$H(z) = 0.5(H_{RR}(z) + \alpha z^{-1}) \tag{4}$$

Here, the transfer function of the longer arm of the MZI is represented by αz^{-1} since the length difference between the two MZI arms is the same as the circumference of the RRs. The phase-shift corresponding to the common length in both arms does not affect the response of the system and is therefore neglected. For lossless system $\alpha = 1$.

Appendix B

In Fig. 2(b), the variables α, α_1, $\theta/2$ and $\theta_1/2$ represent the losses and phase-shift in a half-trip around RR_1 and RR_2, respectively. The interactions of the field components in Fig. 2(b) can be represented with the following equations [36]:

$$E_a = -\kappa^* E_i + t^* \alpha e^{i\theta/2} E_b \tag{5}$$

$$E_b = t_1^* \alpha e^{i\theta/2} E_a - \kappa_1^* \alpha_1 e^{i\theta_1/2} E_{1b} \tag{6}$$

$$E_{1a} = \kappa_1 \alpha e^{i\theta/2} E_a + t_1 \alpha_1 e^{i\theta_1/2} E_{1b} \tag{7}$$

$$E_{1b} = \alpha_1 e^{i\theta_1/2} E_{1a} \tag{8}$$

$$E_t = t E_i + \kappa \alpha e^{i\theta/2} E_b \tag{9}$$

Here, t^* and κ^* represents the complex conjugates.The electric field, E_t, at the output of the serially coupled RRs in Fig. 2(b) can be calculated using the equations above and corresponds to:

$$E_t = E_i \frac{(\alpha^2\alpha_1^2 e^{i(\theta+\theta_1)} - t_1[\alpha^2 e^{i\theta} + t\alpha_1^2 e^{i\theta_1}] + t)}{(t\alpha^2\alpha_1^2 e^{i(\theta+\theta_1)} - t_1[t\alpha^2 e^{i\theta} + \alpha_1^2 e^{i\theta_1}] + 1)} \quad (10)$$

For identical lossless rings, the transfer function of this configuration can be expressed by using $e^{i\theta} = e^{i\theta_1} = z^{-1}$ and $\alpha = \alpha_1 = 1$ as:

$$H_{RR}(z) = \frac{z^{-2} - t_1(1+t)z^{-1} + t}{tz^{-2} - t_1(1+t)z^{-1} + 1} \quad (11)$$

Here, $z^{-1} = e^{-i\beta L}$ corresponds to the propagation for one-trip around the RR as before. The overall transfer function of the filter in Fig. 2(a) can be expressed in terms of the addition of transfer functions in both arms of the MZI as shown in (4).

ACKNOWLEDGMENT

We would like to thank CMC Microsystems for providing access to CAD and LAB tools. In addition, we thank Mohammad Kazemi (ÉTS) for wire-bonding the devices.

REFERENCES

[1] F. Horst, W. M. Green, S. Assefa, S. M. Shank, Y. A. Vlasov, and B. J. Offrein, "Cascaded Mach-Zehnder wavelength filters in silicon photonics for low loss and flat pass-band wdm (de-) multiplexing," *Opt. Exp.*, vol. 21, no. 10, pp. 11652–11658, 2013.

[2] A. Ovvyan, N. Gruhler, S. Ferrari, and W. Pernice, "Cascaded Mach-Zehnder interferometer tunable filters," *J. Opt.*, vol. 18, no. 6, 2016, Art. no. 064011.

[3] O. Schwelb, "A decade of progress in microring and microdisk based photonic circuits: A personal selection," in *Laser Resonators Beam Control X*, vol. 6872. International Society for Optics and Photonics, 2008, Art. no. 68720H.

[4] W. Bogaerts *et al.*, "Silicon microring resonators," *Laser Photon. Rev.*, vol. 6, no. 1, pp. 47–73, 2012.

[5] A. Melloni, "Synthesis of a parallel-coupled ring-resonator filter," *Opt. Lett.*, vol. 26, no. 12, pp. 917–919, 2001.

[6] T. Barwicz *et al.*, "Microring-resonator-based add-drop filters in sin: Fabrication and analysis," *Opt. Exp.*, vol. 12, no. 7, pp. 1437–1442, 2004.

[7] J. C. Mak, A. Bois, and J. K. Poon, "Programmable multiring butterworth filters with automated resonance and coupling tuning," *IEEE J. Sel. Topics Quantum Electron.*, vol. 22, no. 6, pp. 232–240, Nov./Dec. 2016, Art. no. 4402909.

[8] U. Jeong, D. H. Lee, K. Lee, and J. H. Park, "Monolithic 1×8 DWDM silicon optical transmitter using an arrayed-waveguide grating and electro-absorption modulators for switch fabrics in intra-data-center interconnects," *Micromachines*, vol. 11, no. 11, 2020. [Online]. Available: https://www.mdpi.com/2072-666X/11/11/991

[9] A. van Wijk, C. R. Doerr, Z. Ali, M. Karabiyik, and B. I. Akca, "Compact ultrabroad-bandwidth cascaded arrayed waveguide gratings," *Opt. Exp.*, vol. 28, no. 10, pp. 14 618–14 626, May 2020.

[10] C. Klitis, G. Cantarella, M. J. Strain, and M. Sorel, "High-extinction-ratio TE/TM selective Bragg grating filters on silicon-on-insulator," *Opt. Lett.*, vol. 42, no. 15, pp. 3040–3043, Aug. 2017.

[11] W. Shi *et al.*, "Ultra-compact, flat-top demultiplexer using anti-reflection contra-directional couplers for CWDM networks on silicon," *Opt. Exp.*, vol. 21, no. 6, pp. 6733–6738, Mar. 2013.

[12] M. T. Boroojerdi, M. Ménard, and A. G. Kirk, "Wavelength tunable integrated add-drop filter with 10.6 nm bandwidth adjustability," *Opt. Exp.*, vol. 24, no. 19, pp. 22043–22050, Sep. 2016.

[13] T. Zhang, J. Sun, Y. Yang, and Z. Li, "Photonic crystal filter based on defect mode and waveguide mode symmetry matching," *Opt. Commun.*, vol. 428, pp. 53–56, 2018.

[14] A. Melloni and M. Martinelli, "Synthesis of direct-coupled-resonators bandpass filters for WDM systems," *J. Lightw. Technol.*, vol. 20, no. 2, pp. 296–303, 2002.

[15] O. Gerstel, M. Jinno, A. Lord, and S. J. B. Yoo, "Elastic optical networking: A new dawn for the optical layer?," *IEEE Commun. Mag.*, vol. 50, no. 2, pp. s12–s20, Feb. 2012.

[16] C. K. Madsen, "Efficient architectures for exactly realizing optical filters with optimum bandpass designs," *IEEE Photon. Technol. Lett.*, vol. 10, no. 8, pp. 1136–1138, Aug. 1998.

[17] Y. Ding *et al.*, "Bandwidth and wavelength-tunable optical bandpass filter based on silicon microring-mzi structure," *Opt. Exp.*, vol. 19, no. 7, pp. 6462–6470, Mar. 2011.

[18] H. Wang *et al.*, "Polarization-independent tunable optical filter with variable bandwidth based on silicon-on-insulator waveguides," *Nanophotonics*, vol. 7, no. 8, pp. 1469–1477, 2018.

[19] J. C. C. Mak, A. Bois, and J. K. S. Poon, "Programmable multiring butterworth filters with automated resonance and coupling tuning," *IEEE J. Sel. Topics Quantum Electron.*, vol. 22, no. 6, pp. 232–240, Nov.-Dec. 2016.

[20] P. Orlandi, F. Morichetti, M. J. Strain, M. Sorel, P. Bassi, and A. Melloni, "Photonic integrated filter with widely tunable bandwidth," *J. Lightw. Technol.*, vol. 32, no. 5, pp. 897–907, Mar. 2014.

[21] T. Huffman, D. Baney, and D. J. Blumenthal, "High extinction ratio widely tunable low-loss integrated Si_3N_4 third-order filter," 2017, *arXiv:1708.06344*.

[22] I. Lazarou *et al.*, "Bandwidth and wavelength-selective MUX/DEMUX microresonator elements for flexible-grid applications," in *Proc. Adv. Photon.*, Optical Society of America, 2015, p. IT4A.6. [Online]. Available: http://www.osapublishing.org/abstract.cfm?URI=IPRSN-2015-IT4A.6

[23] Q. Sun, L. Zhou, L. Lu, G. Zhou, and J. Chen, "Reconfigurable high-resolution microwave photonic filter based on dual-ring-assisted MZIs on the Si_3N_4 platform," *IEEE Photon. J.*, vol. 10, no. 6, Dec. 2018.

[24] M. S. Rasras *et al.*, "Demonstration of a fourth-order pole-zero optical filter integrated using CMOS processes," *J. Lightw. Technol.*, vol. 25, no. 1, pp. 87–92, 2007.

[25] J. F. Bauters *et al.*, "Ultra-low-loss high-aspect-ratio Si_3N_4 waveguides," *Opt. Exp.*, vol. 19, no. 4, pp. 3163–3174, Feb. 2011.

[26] W. D. Sacher, Y. Huang, G. Lo, and J. K. S. Poon, "Multilayer silicon nitride-on-silicon integrated photonic platforms and devices," *J. Lightw. Technol.*, vol. 33, no. 4, pp. 901–910, 2015.

[27] T. Barwicz *et al.*, "Microring-resonator-based add-drop filters in sin: Fabrication and analysis," *Opt. Exp.*, vol. 12, no. 7, pp. 1437–1442, Apr. 2004.

[28] A. M. Prabhu, A. Tsay, Z. Han, and V. Van, "Extreme miniaturization of silicon add-drop microring filters for VLSI photonics applications," *IEEE Photon. J.*, vol. 2, no. 3, Jun. 2010.

[29] ANSYS, "Lumerical," 2021. [Online]. Available: https://www.lumerical.com/

[30] P. Orlandi, F. Morichetti, M. J. Strain, M. Sorel, A. Melloni, and P. Bassi, "Tunable silicon photonics directional coupler driven by a transverse temperature gradient," *Opt. Lett.*, vol. 38, no. 6, pp. 863–865, Mar. 2013.

[31] J. C. C. Mak, A. Bois, and J. K. S. Poon, "Programmable multi-ring butterworth filters with automated resonance and coupling tuning," in *Proc. Opt. Fiber Commun. Conf.*, Optical Society of America, 2016, p. Tu2F.4.

[32] D. Pérez-López, A. M. Gutierrez, E. Sánchez, P. DasMahapatra, and J. Capmany, "Integrated photonic tunable basic units using dual-drive directional couplers," *Opt. Exp.*, vol. 27, no. 26, pp. 38071–38086, Dec. 2019.

[33] X. Wu *et al.*, "Low power consumption VOA array with air trenches and curved waveguide," *IEEE Photon. J.*, vol. 10, no. 2, Apr. 2018, Art no. 7201308.

[34] Q. Fang *et al.*, "Ultralow power silicon photonics thermo-optic switch with suspended phase arms," *IEEE Photon. Technol. Lett.*, vol. 23, no. 8, pp. 525–527, Apr. 2011.

[35] C. Madsen and J. Zhao, *Optical Filter Design and Analysis: A Signal Processing Approach*. Wiley, 1999.

[36] D. G. Rabus, *Integrated Ring Resonators: The Compendium*. Berlin, Germany: Springer-Verlag, 2007.